ADVANCED ENGINEERING MATERIALS
www.aem-journal.com

High Contrast Thermal Conductivity Change in Ni–Mn–In Heusler Alloys near Room Temperature

Qiye Zheng, Gaohua Zhu,* Zhu Diao, Debasish Banerjee, and David G. Cahill**

Materials with an abrupt transition between a low and a high thermal conductance state at a critical temperature would be useful for thermal regulation applications. Here, the authors report a high contrast reversible thermal conductivity change through the thermally-induced martensitic transition (MT) in Ni–Mn–In alloys. The authors measure the thermal conductivity of a wide temperature range $130 < T < 530$ K using time-domain thermoreflectance (TDTR). The thermal conductivity of these alloys increases from $\approx$7.0–8.5 W m^{-1} K^{-1} to $\approx$11.5–13.0 W m^{-1} K^{-1} through the MT near 300 K as temperature rises, with a rate of change among the highest yet reported in solid-state materials with thermally-induced phase transitions. Based on Hall resistivity measurements, the authors further show that the change of thermal conductivity is dominated by the electronic contribution, which results from a unique carrier mobility change through the MT. Their findings highlight the interplay between the structural disorders and the thermal transport in alloys through solid-state phase transitions and open a new avenue in the search of high-performance materials for thermal regulation.

1. Introduction

A thermal regulator is a nonlinear thermal device or material with an abrupt transition between low and high thermal conductance states at a critical temperature.[1] It can maintain an optimal temperature of an engineering system and may find its way into various thermal management applications such as cryocoolers,[2] vehicle engines, and catalytic converters,[3] as well as waste heat scavengers.[4] Especially, solid-state materials whose thermal conductivity (Λ) increases sharply and reversibly upon heating near room temperature (RT) have attracted intensive attention.[1,5,6] Compared with conventional thermal regulators relying on mechanical forces generated by either differential thermal expansion or changes in the density of materials at a phase transition, material-based solid-state thermal regulators can reduce complexity and improve scalability in engineering designs.[1,4,7]

However, high contrast, solid-state thermal regulators are not yet a reality. Changes in the thermal conductivity of materials with temperature are typically gradual above RT.[8–10] In dielectric crystals, phonons are the dominant heat carriers and typically $\Lambda \propto T^{-1}$ due to anharmonicity. In pure metals, where heat is primarily carried by electrons, Λ is usually almost constant, since the linear increase in electrical resistivity $\rho(T)$ due to electron-phonon scattering is compensated by the increase in temperature as described in the Wiedemann-Franz law $\Lambda_e \approx L(T)T/\rho(T)$ (where Λ_e is the electronic thermal conductivity and $L(T)$ is the Lorenz number).[10] A high contrast change of Λ in a narrow temperature window is often observed in solid state phase transitions, but the high temperature phase rarely has a higher Λ than the low temperature phase. Notable exceptions include the amorphous-to-crystalline transition in chalcogenide glasses (e.g., $Ge_2Sb_2Te_5$, GeAsSe, and As_2Se_3, which is reversible only with extremely fast quenching),[11] the metal-insulator transition (MIT) in some transition metal oxides (e.g., VO_2, $NdNiO_3$, and $La_{1-x}Ca_xMnO_3$),[12–14] the charge density wave (CDW) phase transition in a number of materials (e.g., TaS_2, $TaSe_2$, and $Lu_5Ir_4Si_{10}$),[15] and other structural transitions especially the martensitic transition (MT) in some alloys ($Cu_{2-x}Se$, NiTi, and certain Heusler alloys).[16–18] Although MIT oxides and CDW transition materials exhibit reversible transitions, these materials typically have relatively low Λ even in their high temperature phases, for example, $\approx$6 W m^{-1} K^{-1} in VO_2,[14,19] when compared with metal alloys used in vehicle applications.[20] The relative change of Λ through the transition in known CDW materials is also fairly small (<25%).[15]

Iron shows structural phase transformation as a function of increasing temperature from BCC α-Fe to FCC γ-Fe at

Dr. Q. Zheng, Prof. D.G. Cahill
Department of Materials Science and Engineering
Materials Research Laboratory
University of Illinois at Urbana-Champaign
Urbana, Illinois 61801, USA
E-mail: qzheng9@illinois.edu; d-cahill@illinois.edu
Dr. G.H. Zhu, Dr. D. Banerjee
Materials Research Department
Toyota Research Institute of North America
Ann Arbor, Michigan 48105, USA
E-mail: gaohua.zhu@toyota.com
Dr. Z. Diao
Department of Physics
Stockholm University
SE-106 91 Stockholm, Sweden
Dr. Z. Diao
School of Information Technology
Halmstad University
P.O. Box 823, SE-301 18 Halmstad, Sweden

DOI: 10.1002/adem.201801342

approximately 1180 K followed by transformation from FCC γ-Fe to BCC δ-Fe at approximately 1670 K.[21] The a-to-γ phase transition leads to a kink in the electrical resistivity and a small reduction in Λ of 7% upon heating,[10,22] while the γ-to-δ phase transition at higher temperature induces a small increase in Λ of $<$3%.[10] In Fe-based alloys, such as Fe–Ni and stainless steel HT9, the a-to-γ phase transition temperature can be lowered (e.g., to 900 K) by alloying, but the temperature dependent Λ still shows a small dip through the transition.[23] To the best of our knowledge, the transport properties across the γ-to-δ phase transition in Fe-based alloys have not been reported.

Many off-stoichiometric Ni–Mn–X (X = Ga, In, Sn, Sb) Heusler alloys can transform reversibly between a $L2_1$ cubic high-temperature austenite phase and a less symmetric structurally modulated martensite phase through the MT. Selected compositions of this class of alloys have attracted a lot of attention due to their coupled structural MT and magnetic phase transformation which gives rise to exotic behaviors such as magnetic shape memory effects, magnetocaloric effects, and peculiar magnetic-field-dependent transport properties.[18,24–26] Compared with MIT oxides, off-stoichiometric Ni–Mn–X exhibits a relatively high Λ in the high temperature phase and a fairly small temperature hysteresis ($<$25 K).[18,26,27] In the few previous studies, reversible change of Λ through the MT below RT has been reported in Ni–Mn–In with a considerably larger magnitude when compared with Ni–Mn–Ga.[17,18,26,27] However, in Ni–Mn–In, the mechanism behind the change in Λ and the electrical resistivity through the MT is still under debate and the low MT temperature of materials studied in prior works to a great extent limits their applications.[18,28]

Here, we explore thermal transport across the temperature-induced martensitic phase transition between 320 and 370 K in $Ni_{50}Mn_{50-x}In_x$ alloys with $14 < x < 14.7$ (referred to as Ni–Mn–In below).[29] We use time-domain thermoreflectance (TDTR) to measure the thermal conductivity Λ. The Λ of these alloys increases from $\approx$7.0–8.5 W m^{-1} K^{-1} to $\approx$11.5–13.0 W m^{-1} K^{-1} through the MT, exhibiting 35 to 75% higher Λ in the high-temperature austenite phase in a 50 K window around the transition temperature. Their electrical resistivity also shows a large change from approximately 170 to 220 μm-cm in the martensite phase to $\approx$100 to 130 μm-cm in the austenite phase. The Λ and ρ of the austenite phase between 400 and 500 K are comparable to those for common stainless steels.[20] Analysis based on the Wiedemann-Franz law suggests that the sharp increase in Λ is mainly associated with a surge in the electronic contribution to the thermal conductivity. In contrast to most MIT materials whose electrical resistivity change is induced by a change in charge carrier concentration, our Hall effect measurements show that the electrical resistivity change in Ni–Mn–In is mainly due to a significant difference in the charge carrier mobility between the two phases.

2. Results and Discussion

Polycrystalline Ni–Mn–In alloys were synthesized by arc-melting (see Materials and Methods). Four samples (referred to as sample A, B, C, and D below) with composition listed in **Table 1** are studied. The room temperature crystal structure and purity of the samples in the martensite phase are characterized by X-ray diffraction (XRD) and transmission electron microscopy (TEM) (**Figure 1**a, b). XRD patterns of the four samples are semi-quantitatively analyzed through whole pattern fitting of Rietveld refinement using 6M monoclinic structure with the representative results of sample D shown in Figure 1a (see Figure S1 for the data for other samples). The difference curve (blue line) between the fitting and experimental data shows that no peak is unaccounted for, in good agreement with a previous report.[29] The relatively small difference might be caused by residue austenite phase in the sample or martensite phase of different modulation periods (such as 10 M) which is sensitive to the small composition variation.[29–32] The austenite phase fraction in the sample at room temperature is too low to be accurately identified. Unit cell parameters determined by Rietveld refinement are shown in Table 1.

Bright field high resolution transmission electron microscopy (HRTEM) images of sample D at room temperature (Figure 1b) show that the microstructure of the martensite phase contains at least a two-level hierarchical twin structure. Relatively large twin domains can be seen with widths on the order of tens of nm, while nanoscale twins exist within these large twins. Magnified HRTEM images of the sample (Figure 1c) reveal high density of dislocations around the boundary between two large twins (yellow dashed line). Fast Fourier transformation (FFT) of selected areas in Figure 1c (red dashed squares) suggests that the nanoscale twin boundary lies on the (101) plane and the larger

Table 1. Compiled structure and phase transition results of the Ni–Mn–In alloys.

		Lattice constants at 300 K								
Sample	Composition	a (Å)	b (Å)	c (Å)	β (°)	e/a	T_m (K)	ΔT_m (K)	T_C^M (K)	T_C^A (K)
A	$Ni_{51.7}Mn_{34.3}In_{13.9}$	4.42	5.52	12.90	86.62	8.00	366 (365)	9 (11)	123	303
B	$Ni_{50.7}Mn_{35.0}In_{14.3}$	4.42	5.55	13.02	86.57	7.95	342 (341)	12 (10)	140	302
C	$Ni_{50.3}Mn_{35.6}In_{14.1}$	4.44	5.53	12.95	86.22	7.94	339 (340)	7 (7)	166	315
D	$Ni_{50.3}Mn_{34.8}In_{14.9}$	4.41	5.52	12.93	86.53	7.91	321 (320)	8 (12)	183	307

Compositions of the Ni–Mn–In samples determined by inductively coupled plasma mass spectrometry (ICP-MS) analysis, unit cell parameters from XRD, the valence electron concentrations per atom (e/a), the martensitic transition temperature (T_m) as well as the width of the hysteresis from both electrical resistivity measurements and DSC peaks upon heating and cooling (in parentheses), the Curie temperatures of the martensite phase (T_C^M) and the austenite phase (T_C^A) determined by thermomagnetization curves. Both T_C^M and T_C^A are determined from the arithmetic mean of corresponding peaks in d$M(T)$/dT data upon heating and cooling.

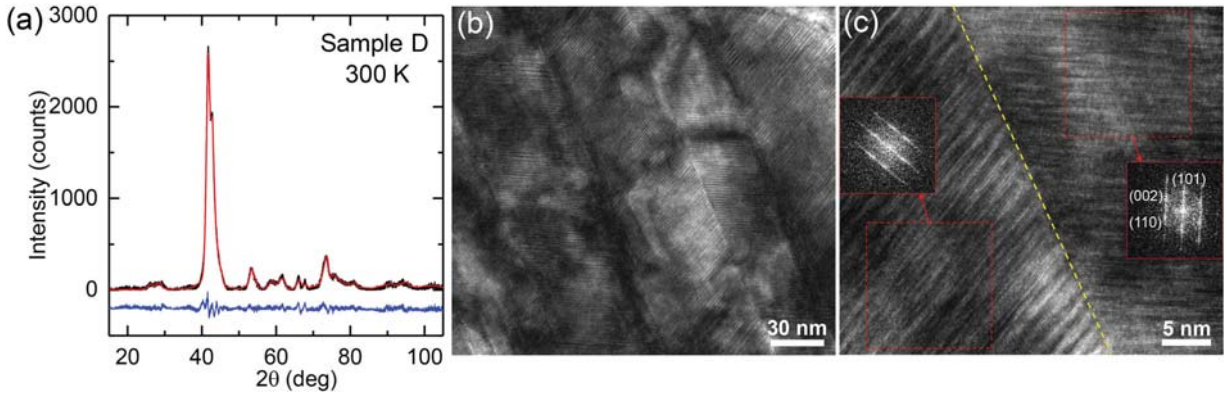

Figure 1. Crystal structure of Ni–Mn–In in the martensite phase. a) X-ray diffraction data (black line), the Rietveld refinements (red line), and the residue (blue line) of the Ni–Mn–In alloys sample D in its martensite phase measured at 300 K. b) HRTEM bright field image of sample D at room temperature showing domains with straight boundaries. c) Magnified HRTEM image showing nanoscale twinning structures. Insets: FFT of the two areas marked by the red dashed squares indexed along the [200] axis. The large-scale twin boundary (yellow dashed line) lies on the (110) plane.

twin boundary is on the (110) plane. In fact, low magnification TEM images as shown in Figure S1 indicate that Ni–Mn–In alloys present a multilevel hierarchical twin structure where very large lamellar domains of a few hundred nm in size with different orientations are visible. Such a complicated structure originates from the low-symmetry monoclinic crystal structure of the martensite phase formed through Bain lattice distortion of the parent austenite phase which contains variants with different possible orientations, leading to a high density of twin boundaries and dislocations.[32] In contrast, the cubic structured austenite phase with higher symmetry are known to have less twin boundaries and other structural defects.[32] The high-density twin boundaries (Figure 1c) is potentially more important in the scattering of electric and heat carriers than dislocations.

The martensitic phase transition of Ni–Mn–In alloys is investigated by temperature dependent XRD (**Figure 2**a) and differential scanning calorimetry (DSC) (Figure 2b). In the DSC scan (between 200 and 460 K), the first order martensitic transition is clearly revealed by the endothermic and exothermic peaks upon heating and cooling, respectively. The crystal structure change through the MT for the representative sample D is also revealed by its dramatically different XRD pattern at 393 K in the austenite phase when compared with that at 300 K in the martensite phase. By Rietveld refinement, the austenite phase is identified as predominantly in the cubic $L2_1$ structure with lattice parameters $a = b = c = 6.00$ Å, while small amount of residual martensite may still exist in the sample.[31]

The martensitic transition temperature (T_m), derived from the arithmetic mean of the peak temperatures in the heating and cooling cycles in DSC, decreases as the In composition increases (see Table 1). T_m in Heusler alloys is related to their electronic structure, which can be effectively accounted for by examining the valence electron concentration, e/a.[33] In the four Ni–Mn–In alloys studied, the range of e/a (≈7.9 to 8.0) and the trend of increasing T_m when e/a increases (Table 1), presumably due to the stabilization of the martensite phases, are consistent with previous work on Ni–Mn–X Heusler alloys.[33,34]

To further characterize the phase transformations and magnetic properties, the temperature dependent magnetization,

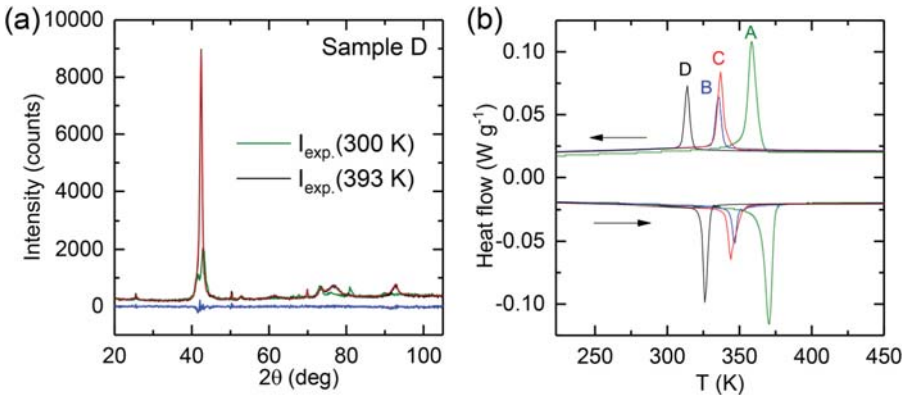

Figure 2. Characterization of the martensitic phase transition in Ni–Mn–In. a) Temperature dependent XRD pattern of sample D at 393 K (black line), the corresponding Rietveld refinements (red line), and the residue (blue line) in comparison with the data at 300 K (green line). The sample is possibly textured in the studied area. b) Differential scanning calorimetry traces of Ni–Mn–In samples between 193 and 473 K. The arrows indicate the heating and cooling cycles. Martensitic transitions appear as endothermic (exothermic) peaks upon heating (cooling).

$M(T)$, of the Ni–Mn–In alloys were characterized from 4 to 390 K upon heating and cooling (**Figure 3**a, b, see Figure S2 for results for sample A and sample B). Upon cooling from 400 K under 10 mT applied field (solid lines), the martensitic transition of the crystal lattice occurs first, corresponding to a change in the magnetization with a hysteresis between the cooling and heating cycle. The measured characteristic transition temperatures, at which the martensite phase starts to appear upon cooling (M_s) and the austenite phase formation finishes upon heating (A_f), are indicated. The MT temperature T_m derived from the arithmetic mean of M_s and A_f is consistent with the T_m obtained from the DSC measurements (Table 1) within 5 K. The increases of magnetization at around 310 K (about 20 K below M_s) is assigned to the Curie temperature of the ferromagnetic (FM) transition in the residual austenite phase, T_C^A, which remains relatively stable in all Ni–Mn–In samples despite their different e/a ratios.[31] The absence of peaks in the DSC curves at T_C^A (Figure 2b) confirms the small fraction of the austenite phase in the martensite matrix and the absence of intermartensitic transition between different martensite structures reported in some literature.[35] The absence of the peak near T_C^A in $M(T)$ under 2 T field (dashed lines in Figure 3b) confirms that the peak at T_C^A in the low field measurement stems from the residue FM austenite phase that saturates in high field rather than another paramagnetic martensite phase, which is consistent with the anomalous Hall resistivity results at low temperatures in **Figure 4**a (see below). Below 200 K, the martensite phase experiences a magnetic phase transition between the paramagnetic and the FM phases at a Curie temperature of T_C^M. A decrease of T_C^M with increasing e/a is observed, in agreement with previous results for Ni-Mn-X Heusler alloys.[33,34]

Figure 3c and d show the longitudinal electrical resistivity (ρ) of Ni–Mn–In alloys samples C and D measured using both a Quantum Design Physical Property Measurement System (PPMS® Dynacool™) and a home-built probe-station, which are consistent within error bars (see Figure S2 for results for samples A and B). We observed an abrupt change in ρ by around 80–100% as temperature decreases through MT with a small hysteresis of 7–12 K (Table 1), in agreement with previous reports.[18,25] The MT temperature T_m observed in the electrical conductivity measurements (using peaks in $d\rho/dT$) are consistent with that observed from both DSC and magnetization measurements. The austenite phase resistivities are around 100 to 130 μΩ-cm, comparable with common NiTi shape memory alloys and stainless steels.[36] At $100 < T < 200$ K, the resistivity of Ni–Mn–In alloys shows a change of slope at around T_C^M due to the change of the electron scattering rate by spin-disorder.[37] Since $T_m > T_C^A$, the weak magnetization which corresponds to negligible spin-disorder scattering of electrons and a high concentration of defects in the austenite phase lead to a flat temperature dependence of ρ at $T > T_m$ with $d\rho/dT$ on the order of 10^{-2} μΩ cm K^{-1}. This trend of $\rho(T)$ in the austenite phase is noticeably different from the case of Ni–Mn–In with $T_m < T_C^A$ in previous studies where the increasing spin-disorder scattering as temperature rises causes $\rho(T)$ to increase rapidly in the austenite phase till T_C^A is reached.[18,26,27] The effect of magnetic field (Figure 3d) and thermal cycling (Figure S2) on electrical resistivity are discussed in the Supporting Information. Further investigation on the mechanism of resistivity change through MT is performed using Hall effect measurements and is presented at the end of this section.

The temperature dependent thermal conductivities, $\Lambda(T)$, for Ni–Mn–In alloys are shown in Figure 3e and f for sample C and sample D, respectively (see Figure S2 for results for samples A and B). The magnitude of Λ increases from ≈7.0 to 8.5 W m^{-1} K^{-1} for the martensite phase at 300 K to ≈12.5 to 14.0 W m^{-1} K^{-1} for the austenite phase at 400 K, showing a distinct jump of 35 to 75% across the MT. In all samples, the MT induced Λ jump occurs above room temperature, in contrast to previous work.[18,26,27] In the temperature range of our study, the Λ away from the MT increases approximately linearly with rising temperature in both the martensite and the austenite phase. The Λ's of the samples in their austenite phase are significantly larger than that of the MIT oxide of VO_2 in its metallic phase (≈6 W m^{-1} K^{-1}) which remains approximately independent of temperature.[14,19] The transition temperature and the thermal hysteresis between heating and cooling in the $\Lambda(T)$ are consistent with the results from $\rho(T)$ measurements.

Generally, for a bulk sample, TDTR is sensitive to the thermal effusivity $(\Lambda C)^{1/2}$ of the sample, and the heat capacity C must be known to extract the thermal conductivity. For the $\Lambda(T)$ data in Figure 3 and S2, the heat capacity values below 300 K were taken from that of $Ni_{49.9}Mn_{35.7}In_{14.4}$ at corresponding temperatures in our analysis and a constant C of 3.37 J cm^{-3} K^{-1} is used at $T > 300$ K to reduce the complexity of the data analysis (see Supporting Information).[38] The change of C above 300 K away from T_m ($|T–T_m| > 10$ K) and the 1–3% difference in the composition of our samples compared with that in literature would lead to <4% error in the result of Λ, smaller than the measurement uncertainty. The real C has a peak at T_m from the latent heat. If the laser induced temperature oscillation in the TDTR measurement is larger than the hysteresis of the phase transition, the heat capacity peak will appear in the analyzed data as a peak in the Λ.[14] The peak during cooling is weaker, in agreement with the heat capacity behavior through the MT as a 1st order phase transition.[39] Due to a low fraction of the austenite phase, we do not observe a sharp peak near T_C^A. We note the $\Lambda(T)$ at the close vicinity of T_m ($< \pm 5$ K) is not the focus of this work.

There is variation in Λ from measurements performed at different locations on the same sample near T_m, but it becomes far less pronounced around 50 K above T_m. We attribute this variation to the small chemical or structural inhomogeneity in the regions probed by the TDTR measurement (see Supporting Information), which is consistent with the existence of a small amount of residual martensite phase in the XRD pattern at 393 K, as shown in Figure 2a.[30,32,35]

We estimate the electronic thermal conductivity by the Wiedemann-Franz law $\Lambda_e \approx L(T)T/\rho(T)$. Since our measurements focus on the high temperature limit, $T \geq \Theta_D \approx 316K$ for Ni–Mn–In (Θ_D is the Debye temperature),[36] and the high defect concentration in Ni–Mn–In alloys may lead to strong elastic scattering of electrons,[8] we took the Sommerfeld value of Lorenz number $L(T) = L_0 = 2.44 \times 10^{-8}\,\Omega\,W\,K^{-2}$. As shown in Figure 3e and f, the change in the total thermal conductivity Λ is dominated by the electronic contribution Λ_e which experiences approximately the same magnitude of abrupt change through the MT. In contrast, the phonon thermal

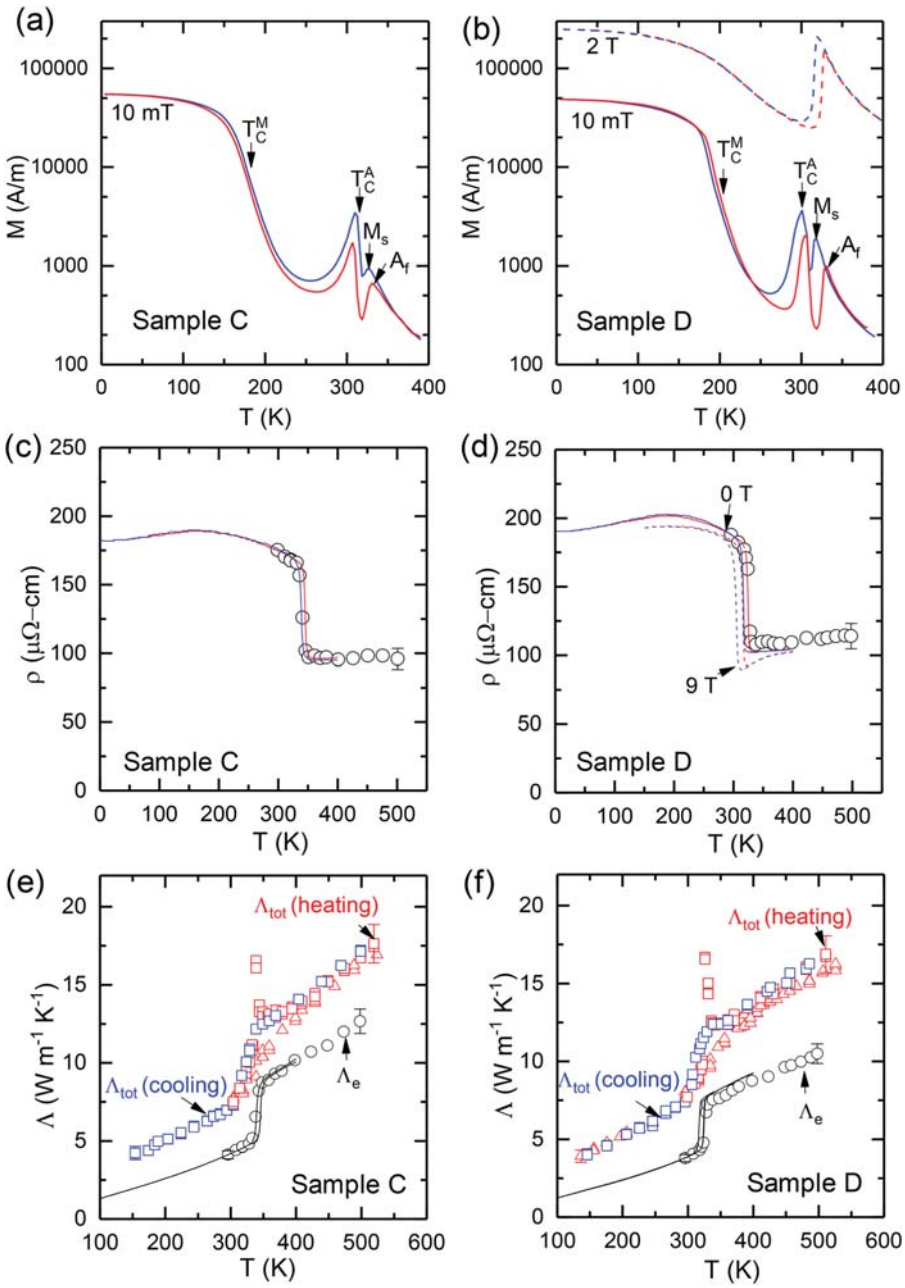

Figure 3. Magnetization and electrical and thermal transport properties as a function of temperature in Ni–Mn–In. Temperature dependent magnetization, $M(T)$, of Ni–Mn–In alloys sample C (a) and sample D (b) in an applied field of 10 mT between 4 and 390 K (solid lines). Dashed lines in panel (b) are $M(T)$ measured under 2 T field. Red lines are recorded during heating cycles and blue lines are during cooling cycles. The temperatures at which the martensite phase starts to appear (M_s), the austenite phase formation finishes (A_f), and the Curie temperature of the martensite (T_C^M) and the austenite (T_C^A) phases are labeled. c) and d) Temperature dependence of longitudinal electrical resistivity of sample C and D, respectively. The results obtained through thermal cycling on a PPMS between 4 and 400 K (red solid lines for heating, blue solid lines for cooling) are shown together with measurements using a probe-station upon heating from 300 to 500 K (black open circles). The dashed line in (d) is a PPMS measurement of sample D in 9 T magnetic field. Representative error bars in the probe station measurement are also shown. e) and f) The thermal conductivity Λ of sample C and D, respectively, between 150 and 530 K upon heating (red open squares and red open triangles) and cooling (blue open squares). Different red symbols represent data from the heating cycle collected from different locations on the same samples. The cooling curve is obtained at the same location as heating curve represented with squares. Electronic thermal conductivity Λ_e calculated from the measured electrical conductivity on the PPMS (black lines) and on the probe station (open circles) using the Wiedemann-Franz law are also shown. Representative error bars in Λ's are provided.

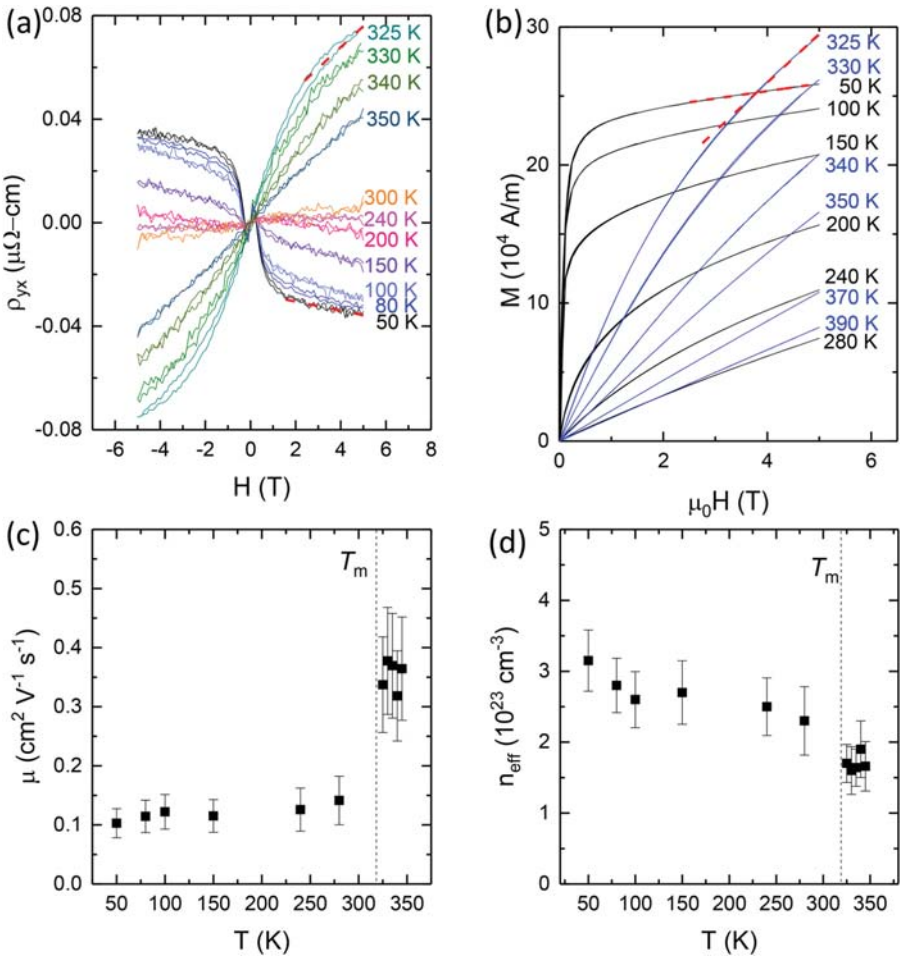

Figure 4. Hall effect and field dependent magnetization studies of Ni–Mn–In. a) Hall resistivity of sample D at several temperatures below and above the MT between −5 and 5 T. b) Field dependent magnetization of sample D at temperatures corresponding to panel (a) between −5 and 5 T. The martensite phase and the austenite phase data are plotted with black lines and blue lines, respectively. Representative linear curve fittings of the high field data at 325 K and 50 K are shown in panels (a) and (b). c) Hall mobility as a function of temperature between 50 and 345 K calculated using carrier concentration in panel (d) and resistivity in **Figure 3**d. d) Effective carrier concentration obtained from $n_{eff} = -\frac{1}{R_0 e}$ as a function of temperature between 50 and 345 K obtained from Hall resistivity and M versus H results using Equation (2) and (3).

conductivity ($\Lambda_{ph} = \Lambda - \Lambda_e$) remains roughly constant at around 3 to 5 $W m^{-1} K^{-1}$ in different samples (See Figure S3 for the result of Λ_{ph} from 280 to 420 K). Hence, we attribute the increases in the thermal conductivity of Ni–Mn–In through martensitic transition to a change of the electronic contribution.

The weak temperature dependence of $\rho(T)$ in the austenite phase, due to large residual resistivity and almost negligible spin-disorder scattering, leads to a nearly linear increase of Λ_e and hence Λ with temperature following the Wiedemann-Franz law. By contrast, in previous studies of Ni–Mn–In alloys with T_m below RT and T_C^A, $\rho(T)$ increases with temperature above T_m due to increasing spin-disorder scattering in the FM austenite phase, and correspondingly, Λ shows weak temperature dependence below T_C^A.[18,25] We also note that all previous data of $\Lambda(T)$ for Ni–Mn–In from literature that we are aware of (measured with the static state method) shows abrupt changes of slope or unidentified peaks above 300 K (in the austenite phase of their samples), which are neither explained nor discussed in those papers.[18,26,27]

The longitudinal electrical resistivity, that is, the diagonal term of the resistivity tensor, can be expressed as $\rho_{ii} = (nq\mu)^{-1}$, ($i = x$, y, z) where n is the carrier concentration, μ the carrier mobility, and q the elementary charge of the carrier. In general, n depends on electron density of states, and μ is roughly proportional to the average carrier relaxation time $\langle\tau\rangle$, which is determined by the scattering processes. Both n and μ may be influenced by the MT in Ni–Mn–In, which changes the electronic structure and the structural disorder.[32,40]

To better understand the mechanism behind the change of electrical and thermal conductivity through the MT, we combine Hall effect measurements and field-dependent magnetization measurements at different temperatures on sample D (see Figure 4). In ferromagnetic materials, with electric current applied along the x direction and the applied magnetic field H along the z direction, the transverse Hall resistivity ρ_{yx} measured

along the y direction (as an off-diagonal term in the resistivity tensor) is generally expressed as

$$\rho_{yx}(H) = R_0 B_z(H) + R_s \mu_0 M_z(H), \quad (1)$$

where the first term describes the normal Hall effect (NHE) arising from the influence of the Lorentz force, characterized by the normal Hall coefficients, R_0. The second term characterized by the coefficient R_s describes the anomalous Hall effect (AHE) in materials with spontaneous magnetization M_z (along the z axis, μ_0 is the vacuum permeability), as a consequence of spin-orbit interactions which typically involve coherent band mixing effects from both the external electric field and disorders.[41,42] B_z is the magnetic induction which is usually given by $B_z = \mu_0 H + \mu_0 M_z(1-N)$, where $0 \leq N \leq 1$ is the demagnetizing factor of the sample. We estimate the demagnetizing factor N of the sample to be around 0.63 based on its geometry.[43]

The magnetization is typically related to the applied field as $M_z = \chi_1 H$ at low field, $H \ll NM_s$, and $M_z = \chi_2 H + M_s$ at large fields, $H > NM_s$, where χ_1 and χ_2 are corresponding susceptibilities and M_s is the saturation magnetization (typically $\chi_1 \gg \chi_2$). At temperatures when there is a change of slope in $\rho_{yx}(H)$ and $M_z(H)$, R_0 and R_s can be determined using the data in the high field regime by the method described in Materials and Methods.

The M versus H curves at corresponding temperatures are shown in Figure 4b. At low temperatures (<200 K), the magnetization of the sample in the martensite phase shows FM behavior with saturation at high fields (>1 T), in agreement with the M versus T data in Figure 3a and b. The small hysteresis loop in $\rho_{yx}(H)$ curves below 0.2 T could be attributed to a second FM phase in the martensite which is likely the residue FM austenite owing to its large AHE coefficient R_s. At a temperature above T_m in the austenite phase, both Hall resistivity and magnetization show a change of slope at around 2 T and do not saturate. This might be related to the presence of superparamagnetism in the austenite phase.[44]

We used the method described in the Materials and Methods at high fields ($3.5\,\mathrm{T} < \mu_0|H| < 5\,\mathrm{T}$ for the austenite phase and between $2.5\,\mathrm{T} < \mu_0|H| < 5\,\mathrm{T}$ for the martensite phase) to estimate the normal Hall coefficient R_0. The measured R_0 is consistently negative, corresponding to electron-type carriers, with values between $\approx -2 \times 10^{-11}$ and $\approx -4 \times 10^{-11}\,\mathrm{m^3\,C^{-1}}$ in the temperature range of 50 to 345 K with a small change near T_m (see Figure S5) to have larger even magnitude in the austenite phase, comparable with the magnitude of that of Al ($-3.4 \times 10^{-11}\,\mathrm{m^3\,C^{-1}}$), Pt ($-2.3 \times 10^{-11}\,\mathrm{m^3\,C^{-1}}$), Ir ($+3.2 \times 10^{-11}\,\mathrm{m^3\,C^{-1}}$), and Ni_2MnSn Heusler alloys ($L2_1$ structure, $+2.67 \times 10^{-11}\,\mathrm{m^3\,C^{-1}}$).[41,45]

The Hall mobility μ_H for sample D is obtained from the NHE coefficient and the longitudinal electrical resistivity in Figure 3d using $\mu_H = |R_0/\rho_{xx}|$. As shown in Figure 4c, μ_H changes by a factor of 2 to 3 across the MT. The change in mobility could be attributed to the increase of scattering rate of carriers with an increased density of structural defects in the martensite phase with a low-symmetry modulated monoclinic structure compared with the high-symmetry cubic structured austenite phase.[32] The nanoscale twin boundaries as shown in Figure 1b and c in the martensite phase may strongly reduce the mean free path of electrons in Ni–Mn–In which should be on the order of a few nanometer, smaller than elemental FM metals.[46] To the best of our knowledge, such an increase in electrical thermal conductivity as a consequence of an abrupt increase in carrier mobility due to the change of structural disorder through a martensitic transition has not been reported previously in solid-state phase transition materials. The higher defect concentration in the martensite phase is also evidenced by the larger residual electrical resistivity as shown in Figure 3d. Considering the small kink in ρ_{xx} at T_C^M where large change of magnetization occurs, we do not expect the change in spin-disorder scattering from the relatively small change of magnetization at T_m to be strong enough to explain the behavior of μ_H through the MT. Thus, the thermal conductivity change through the MT in Ni–Mn–In is mainly a result of change in electrical mobility, which is different from that through the MIT in VO_2 where changes in carrier concentration dominate.[14,19] The reduction of disorder in the austenite phase and a weakly temperature-dependent carrier concentration can also explain the small increase in phonon thermal conductivity through the MT (Figure S3).

Assuming some of the unfilled bands near the Fermi surface have closed orbits and one type of carriers make predominant contribution to the Hall effect (with net effective carrier concentration n_{eff}), R_0 can be expressed as $R_0 = -\frac{1}{n_{eff}\,q}\frac{\langle\tau^2\rangle}{\langle\tau\rangle^2}$, under low field limit $\mu_H B \ll 1$ (In our case, μ_HB is on the order of 10^{-4}).[41,47] In the absence of any detailed knowledge of the scattering mechanism and Fermi surface geometry that determine the average relaxation time, we make the approximation of $\frac{\langle\tau^2\rangle}{\langle\tau\rangle^2} = 1$ (which typically varies between 1 and 2). The carrier concentration in Ni–Mn–In sample D between 50 and 345 K (Figure 4d) shows no significant change through the MT and is even slightly lower in the austenite phase with values comparable with that of Ni_2MnSn Heusler alloys, $2.3 \times 10^{23}\,\mathrm{cm^{-3}}$.[41] According to previous theoretical and photoelectron studies of Ni–Mn–In, the modification of the density of states (DOS) from the lattice structure change through the MT is rather insignificant within k_BT of the Fermi level.[40,48] The reported increase in the electron carrier concentration in $Ni_{50}Mn_{34}In_{16.3}$ in a previous work, deduced from low temperature heat capacity measurements, is questionable since the same carrier effective mass is assumed for both the austenite and the martensite phase.[18]

The high contrast change of thermal conductivity in Ni–Mn–In alloy is repeatable. We perform thermal cycle test by heating and cooling the sample D at a rate of $15\,\mathrm{K\,min^{-1}}$ between 295 and 395 K using the same heater stage for the temperature dependent TDTR measurement. After 25 cycles, the measured $\Lambda(T)$ at approximately the same location of the sample upon heating from 300 to 420 K shows no observable difference from the results measured before the cycling (Figure S4). According to a prior study, the effect of thermal cycling on $\rho(T)$ in Ni–Mn–In tends to appear after more than 500 cycles due to the build-up of dislocation density in both phases.[49] In addition, we test the effect of fast heating at a rate of $100\,\mathrm{K\,min^{-1}}$ from 300 to 500 K and quenching from 500 K in liquid nitrogen for sample C and D. Neither of the processes leads to observable change of Λ in the martensite phase at 300 K and austenite phase at 400 K.

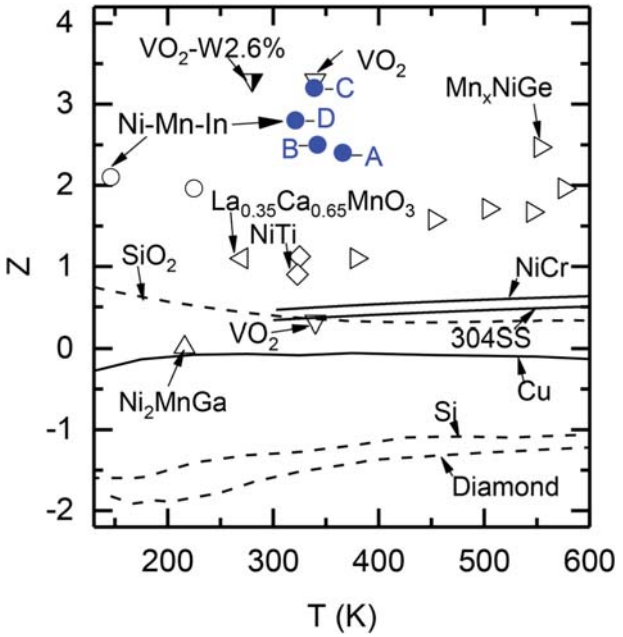

Figure 5. Logarithmic rate of change in thermal conductivity, Z, for Ni–Mn–In alloys in comparison with other materials. Ni–Mn–In (blue filled circles from this work and black open circles from references,(26, 19) Cu,[51] 304 stainless steel,[20] Ni–22at%Cr alloy,[52] Si,[53] SiO_2,[54] natural type-IIa diamond,[55] NiTi,(20, 60) VO_2 thin film (upper open triangle) and single crystal nanobeam (lower open triangle) and VO_2–W2.6% nanobeam,(14, 21) $La_{0.35}Ca_{0.65}MnO_3$,[13] Mn_xNiGe,[56] and Ni_2MnGa.(*18*)

To evaluate the MT induced thermal conductivity change in Ni–Mn–In alloys for thermal regulator applications, we define an average logarithmic rate of change in thermal conductivity in a certain temperature range as: $Z(T) = \frac{\partial \ln \Lambda}{\partial \ln T}$. The larger the absolute value of Z the faster the change in thermal conductivity. For materials with phase transitions, we calculate the average value of $\langle Z \rangle = \langle \frac{\partial \ln \Lambda}{\partial \ln T} \rangle \approx \langle \frac{T}{\Lambda} \frac{\Delta \Lambda}{\Delta T} \rangle$ in the range of approximately $T^* \pm 25$ K, where T^* is their correponding phase transition temperatures. The sharp peaks in Λ for Ni–Mn–In within a 5 K near T_m (Figure 3) is excluded in the calculation. The largest value of $\langle Z \rangle$ is used if multiple data sets exist.

The data of $\langle Z \rangle$ for Ni–Mn–In alloys in this work, $Z(T)$ for some common materials without phase transition, and $\langle Z \rangle$ for materials with a thermally-induced phase transition between 150 and 600 K are illustrated in **Figure 5**. Z values for phase transition materials of NiTi, VO_2, and Ni–Mn–In are positive and larger than alloys without phase trantions as a result of the sharp change in thermal conductivity within a narrow temperature window. Among MT materials,$\langle Z \rangle$ for Ni–Mn–In is larger than that for NiTi, Ni_2MnGa, and Mn_xNiGe. Compared with MIT materials, $\langle Z \rangle$ for Ni–Mn–In are higher than that of $La_{0.35}Ca_{0.65}MnO_3$ and comparable with that of VO_2 thin films. The largest value of Z is around 3.2 for Ni–Mn–In sample C which means a 10% change in temperature would lead to ≈30% change in thermal conductivity around the transition temperature. Ni–Mn–In shows the fastest rate of change in thermal conductivity among all materials examined. Although VO_2 thin films and W doped VO_2 nanobeams exhibit comparable rate of change, pure VO_2 single crystal nanobeams show much smaller $\langle Z \rangle$.

3. Conclusion

We measured the high contrast thermal conductivity change across thermally induced martensitic phase transitions in Ni–Mn–In alloys from 130 to 530 K using time-domain thermoreflectance (TDTR). The average rate of change of Λ in Ni–Mn–In in a 50 K range around their transition temperatures is faster than common metals and alloys including the conventional NiTi shape memory alloy and it is comparable with VO_2. The austenite phase thermal and electrical conductivity near 400 K for Ni–Mn–In are more than twice as large as that for VO_2 in its metallic state and comparable with that for stainless steels. By comparing the result with the electronic thermal conductivity calculated from the Wiedemann-Franz law, and Hall effect studies, we attribute such a rapid change in the thermal conductivity to the electronic contribution which is modified by a large change in the carrier mobility through the martensitic transition. Our work sheds light upon the important interplay between the dynamic change of structural disorder and the change of electrical and thermal transport properties in solid-state phase transitions and will help guide the development of future thermal regulation materials.

4. Experimental Section

Sample Preparation: Polycrystalline $Ni_{50}Mn_{50-x}In_x$ ($x = 14.0$, 14.3, 14.5, and 14.7) alloys were prepared using arc melting under argon atmosphere. During the arc melting process, Ni and Mn were melted first, and then the ingot was melted within three times. Subsequently, the ingot was sealed in an evacuated quartz tube and annealed at 1073 K for 24 h, followed by natural cooling down to room temperature. To determine the actual compositions in samples, inductively coupled plasma mass spectroscopy (ICP-MS) measurements are performed. The measured compositions are in reasonable agreement with the nominal compositions (see Table 1).

Structure Characterization: The X-ray diffraction is conducted at room temperature using a Bruker D8 Vantec micro-diffractometer equipped with a micro-focus copper x-ray tube with Montel optics monochromator, a 0.5 mm secondary collimator, a Vantec 500 2-D area detector and laser alignment system. During a coupled Theta/2Theta scan, the sample stage was oscillated in the *x* and *y* directions and rotated in the Phi direction around the area of interest to increase the number of crystallites brought into diffracting conditions.

The high temperature X-ray diffraction is conducted using a Rigaku Smartlab diffractometer. The samples were placed on a silicon zero background plate inside the Rigaku high temperature furnace on the diffractometer for the XRD measurement.

TEM specimen of the bulk Ni–Mn–In alloys were prepared using an in-situ FIB lift-out technique on a FEI Dual Beam FIB/SEM. The HRTEM images were obtained using a FEI Tecnai TF20 FEG/TEM.

Phase Transitions Characterization: The phase transformation behavior was measured by modulated differential scanning calorimetry using a TA Instruments DSC 250. The samples were loaded in an aluminum pan and were scanned using a sinusoidal temperature modulation in the range of 188–473 K with a linear ramp rate of 3 K min^{-1}.

The temperature and field dependencies of the sample magnetization are studied using a superconducting quantum interference device (SQUID) magnetometer (Quantum Design Magnetic Property Measurement System MPMS®3).

Electrical and Thermal Transport Properties Characterization: To prepare a smooth surface for TDTR measurements, the sample is cut into thin

plates of 0.1–0.4 mm by a wire saw, mechanically polished, and then coated with Al by DC magnetron sputtering. We pay extreme attention to the smoothness of the sample surface. We compare its reflectivity at 785 nm laser wavelength with that of an Al coated silicon wafer. The Al coating for the Ni–Mn–In alloy sample and the silicon wafer are carried out in the same sputtering run. Only samples showing a reflectivity >95% of that of the Al coated silicon wafer are selected for TDTR characterization.

Time-domain thermoreflectance method was used to measure the thermal conductivity of Ni–Mn–In alloys.[29] In a TDTR measurement, a train of optical pulses at a repetition rate of 80 MHz, generated by a mode-locked Ti:Sapphire laser at a wavelength of 785 nm, is split into separate pump and probe beams with the optical path of the pump beam controlled by a mechanical delay stage. The pump beam is modulated at a frequency of 9.1 MHz by an electro-optical modulator. The pump and probe beams are focused on the sample through a 5× objective lens to a $1e^{-2}$ intensity radius of ≈10.1 μm.[57] The changes in the intensity of the reflected probe beam created by the pump beam are measured using phase-sensitive lock-in detection. The ratio of the in-phase (V_{in}) and out-of-phase (V_{out}) signal from the lock-in amplifier is then fit to a thermal diffusion model obtained from an analytical solution for heat flow in a layered structure.[29] See Supporting Information for more details.

The electrical resistivity of the Ni–Mn–In samples is measured by the van der Pauw method using a Stanford Research System SR830 lock-in amplifier and a home-built probe station equipped with Signatone tungsten carbide probes. A custom-made circuit is used to switch the current/voltage contacts as well as reverse the bias polarity. Typically, a 1.00 V(rms), 13 Hz sine wave output is applied to the circuit, which is converted to a 6.7 mA(rms) bias current through the sample using a total bias resistance of 150 Ω. To eliminate any residual phase error, we measured a 20 nm platinum film on sapphire and set the phase to a value (typically ≈0.6 deg) to minimize the out-of-phase reading. Using this setup, we measured the resistivity of an 80 nm Al film on thermally oxidized Si wafer to be 3.27 μΩ-cm. This is consistent with the result of 3.31 μΩ-cm measured by a commercial Signatone collinear four-point probe connected to a Keithley 2000 multimeter. We also measured a resistivity of 72 μΩ-cm for a 304 stainless steel, which is in agreement with the literature value of 74 μΩ-cm.

The electrical resistivity of all Ni–Mn–In samples are also measured in a Quantum Design physical property measurement system (PPMS® Dynacool™) using the van der Pauw method with 8 mA bias current. As the PPMS system only has two signal channels for resistance measurements, samples are measured in the van der Pauw geometry without switching the side of current and voltage. The PPMS data is then re-scaled by matching the room temperature result with that measured on the probe station. The scaling factor takes account of the nonideality of the shape of the sample. The major sources of error in the resistivity obtained from both methods are the sample thickness variation (3–6%) and the location of the probes or contacts (1–3%). The error in the bias resistance (1%) also contributes to the total error in the probe station measurement which amounts to about 6% in total.

Hall Effect Measurements: Hall effect measurements are carried out on sample D, cut into a 0.35 × 0.7 × 10 mm strip, by the four probe bar method[50] on the Quantum Design PPMS with magnetic field swept between ±5 T and a temperature range from 50 to 370 K. A SR830 lock-in amplifier was used to apply low frequency ac current and perform phase-sensitive detection. A 3.00 V(rms), 43 Hz sine wave output is converted to a 30 mA(rms) bias current through the sample using a total bias resistance of 100 Ω. The transverse Hall resistivity is measured through an SR554 transformer preamplifier with 500× amplification to provide a good "noise matching" to the sample impedance.

The Hall resistivities at a series of temperatures for Ni–Mn–In sample D are shown in Figure 4a, where we used the asymmetric components of the raw experimental data $\rho_{yx}(H) = \frac{1}{2}\left(\rho_{yx}^{exp}(+H) - \rho_{yx}^{exp}(-H)\right)$ to subtract the magnetoresistance (which is typically an even function of the applied magnetic field).[41]

Using the expression for B_z and M_s, the Hall resistivity can be rewritten as

$$\rho_{yx}^{LF}(H) = (R_0\mu_0(1+\chi_1(1-N)) + R_s\mu_0\chi_1)H, \text{ when } H \ll NM_s \quad (2)$$

and

$$\rho_{yx}^{HF}(H) = (R_0\mu_0(1+\chi_2(1-N)) + \chi_2 R_s\mu_0)H + R_0\mu_0 M_s(1-N) + R_s\mu_0 M_s, \text{ when } H > NM_s. \quad (3)$$

At temperatures where the Hall resistivity versus field shows a saturation behavior or a change of slope, R_s and R_0 can be obtained from the intercept and slope of a linear fitting of $\rho_{yx}^{HF}(H)$ at high fields, using the susceptibilities of χ_2 measured separately from M versus H curves.

Supporting Information

Supporting Information is available from the Wiley Online Library or from the author.

Acknowledgements

Research on the electrical and thermal transport properties and magnetic properties were carried out in the Frederick Seitz Materials Research Laboratory Central Research Facilities, University of Illinois. This project was supported by Toyota Motor North America (TMNA) and partially supported by the National Science Foundation MRSEC program under NSF Award Number DMR-1720633. Z.D. acknowledged support from the Swedish Research Council (VR) under grant number 2015–00585, co-funded by Marie Skłodowska-Curie Actions (Project INCA 600398).

Conflict of Interest

The authors declare no conflict of interest.

Keywords

Hall mobility, Heusler alloys, martensitic transition, thermal conductivity regulation, time-domain thermoreflectanc

Received: December 17, 2018
Revised: January 25, 2019
Published online:

[1] G. Wehmeyer, T. Yabuki, C. Monachon, J. Wu, C. Dames, *Appl. Phys. Rev.* **2017**, *4*, 041304.
[2] M. Dietrich, A. Euler, G. Thummes, *Cryogenics* **2014**, *59*, 70.
[3] M. Gumus, *Appl. Therm. Eng.* **2009**, *29*, 652.
[4] R. McCarty, D. Monaghan, K. Hallinan, B. Sanders, *J. Thermophys. Heat Transfer* **2007**, *21*, 505.
[5] C. Li, Y. Ma, Z. Tian, *ACS Macro Lett.* **2017**, *7*, 53.
[6] G. Zhu, J. Liu, Q. Zheng, R. Zhang, D. Li, D. Banerjee, D. G. Cahill, *Nat. Commu.* **2016**, *7*, 13211.
[7] a) J. Franco, D. Martins, I. Catarino, G. Bonfait, *Appl. Therm. Eng.* **2014**, *70*, 115; b) R. Kandasamy, X.-Q. Wang, A. S. Mujumdar, *Appl. Therm. Eng.* **2008**, *28*, 1047.

[8] Q. Zheng, A. B. Mei, M. Tuteja, D. G. Sangiovanni, L. Hultman, I. Petrov, J. E. Greene, D. G. Cahill, *Phys. Rev. Mater.* **2017**, *1*, 065002.
[9] R. Powell, C. Y. Ho, P. E. Liley, *Thermal Conductivity of Selected Materials*, Vol. *8*, US Government Printing Office, Washington, DC **1966**.
[10] C. Y. Ho, R. W. Powell, P. E. Liley, *J. Phys. Chem. Ref. Data* **1972**, *1*, 279.
[11] a) H.-K. Lyeo, D. G. Cahill, B.-S. Lee, J. R. Abelson, M.-H. Kwon, K.-B. Kim, S. G. Bishop, B.-K. Cheong, *Appl. Phys. Lett.* **2006**, *89*, 151904; b) A. B. Seddon, *J. Non-Cryst. Solids* **1995**, *184*, 44.
[12] M. K. Hooda, C. S. Yadav, *Physica B* **2016**, *491*, 31.
[13] J. Cohn, J. Neumeier, C. Popoviciu, K. McClellan, T. Leventouri, *Phys. Rev. B* **1997**, *56*, R8495.
[14] D.-W. Oh, C. Ko, S. Ramanathan, D. G. Cahill, *Appl. Phys. Lett.* **2010**, *96*, 151906.
[15] a) M. Núñez-Regueiro, J. Lopez-Castillo, C. Ayache, *Phys. Rev. Lett.* **1985**, *55*, **1931**; b) Y. K. Kuo, C. S. Lue, F. H. Hsu, H. H. Li, H. D. Yang, *Phys. Rev. B* **2001**, *64*, 125124.
[16] a) H. Liu, X. Shi, F. Xu, L. Zhang, W. Zhang, L. Chen, Q. Li, C. Uher, T. Day, G. J. Snyder, *Nat. Mater.* **2012**, *11*, 422; b) B. D. Ingale, W. C. Wei, P. C. Chang, Y. K. Kuo, S. K. Wu, *J. Appl. Phys.* **2011**, *110*, 113721.
[17] Y. K. Kuo, K. M. Sivakumar, H. C. Chen, J. H. Su, C. S. Lue, *Phys. Rev. B* **2005**, *72*, 054116.
[18] B. Zhang, X. X. Zhang, S. Y. Yu, J. L. Chen, Z. X. Cao, G. H. Wu, *Appl. Phys. Lett.* **2007**, *91*, 012510.
[19] S. Lee, K. Hippalgaonkar, F. Yang, J. Hong, C. Ko, J. Suh, K. Liu, K. Wang, J. J. Urban, X. Zhang, *Science* **2017**, *355*, 371.
[20] R. S. Graves, T. G. Kollie, D. L. McElroy, K. E. Gilchrist, *Int. J. Thermophys.* **1991**, *12*, 409.
[21] R. Boehler, *Rev. Geophys.* **2000**, *38*, 221.
[22] L. Deng, C. Seagle, Y. Fei, A. Shahar, *Geophys. Res. Lett.* **2013**, *40*, 33.
[23] a) J. Terpiłowski, R. Rudzki, R. Szczepaniak, G. Woroniak, *J. Alloys Compd.* **2018**, *735*, 560; b) L. Leibowitz, R. Blomquist, *Int. J. Thermophys.* **1988**, *9*, 873.
[24] a) R. Kainuma, Y. Imano, W. Ito, Y. Sutou, H. Morito, S. Okamoto, O. Kitakami, K. Oikawa, A. Fujita, T. Kanomata, *Nature* **2006**, *439*, 957; b) S. J. Murray, M. Marioni, S. M. Allen, R. C. O'Handley, T. A. Lograsso, *Appl. Phys. Lett.* **2000**, *77*, 886.
[25] S. Yu, Z. Liu, G. Liu, J. Chen, Z. Cao, G. Wu, B. Zhang, X. Zhang, *Appl. Phys. Lett.* **2006**, *89*, 162503.
[26] A. B. Batdalov, A. M. Aliev, L. N. Khanov, V. D. Buchel'nikov, V. V. Sokolovskii, V. V. Koledov, V. G. Shavrov, A. V. Mashirov, E. T. Dil'mieva, *J. Exp. Theor. Phys.* **2016**, *122*, 874.
[27] L. S. S. Chandra, M. K. Chattopadhyay, V. K. Sharma, S. B. Roy, S. K. Pandey, *Phys. Rev. B* **2010**, *81*, 195105.
[28] A. Granovskii, V. Prudnikov, A. Kazakov, A. Zhukov, I. Dubenko, *J. Exp. Theor. Phys.* **2012**, *115*, 805.
[29] a) D. G. Cahill, *Rev. Sci. Instrum.* **2004**, *75*, 5119. b) Q. Zheng, S. Li, C. Li, Y. Lv, X. Liu, P. Y. Huang, D. A. Broido, B. Lv, D. G. Cahill, *Adv. Func. Mater.* **2018**, *28*, 1805116. c) S. Li, Q. Zheng, Y. Lv, X. Liu, X. Wang, P. Y. Huang, D. G. Cahill, B. Lv, *Science* **2018**, *361*, 579. d) Q. Zheng, C. Li, A. Rai, J. H. Leach, D. A. Broido, D. G. Cahill, *Phys. Rev. Mater.* **2019**, *3*, 014601.
[30] H. Yan, Y. Zhang, N. Xu, A. Senyshyn, H.-G. Brokmeier, C. Esling, X. Zhao, L. Zuo, *Acta Mater.* **2015**, *88*, 375.
[31] T. Krenke, M. Acet, E. F. Wassermann, X. Moya, L. Mañosa, A. Planes, *Phys. Rev. B* **2006**, *73*, 174413.
[32] H. Sepehri-Amin, A. Taubel, T. Ohkubo, K. P. Skokov, O. Gutfleisch, K. Hono, *Acta Mater.* **2018**, *147*, 342.
[33] P. Antoni, M. Lluís, A. Mehmet, *J. Phys.* **2009**, *21*, 233201.
[34] T. Krenke, X. Moya, S. Aksoy, M. Acet, P. Entel, L. Mañosa, A. Planes, Y. Elerman, A. Yücel, E. F. Wassermann, *J. Magn. Magn. Mater.* **2007**, *310*, 2788.
[35] Y. Wu, S. Guo, S. Yu, H. Cheng, R. Wang, H. Xiao, L. Xu, R. Xiong, Y. Liu, Z. Xia, C. Yang, *Sci. Rep.* **2016**, *6*, 26068.
[36] V. Antonucci, G. Faiella, M. Giordano, F. Mennella, L. Nicolais, *Thermochim. Acta* **2007**, *462*, 64.
[37] B. R. Coles, *Adv. Phys.* **1958**, *7*, 40.
[38] J.-H. Chen, N. M. Bruno, I. Karaman, Y. Huang, J. Li, J. H. Ross Jr., *Acta Mater.* **2016**, *105*, 176.
[39] S. M. Podgornykh, E. G. Gerasimov, N. V. Mushnikov, T. Kanomata, *J. Phys.* **2011**, *266*, 012004.
[40] S. W. D'Souza, A. Chakrabarti, S. R. Barman, *J. Electron Spectrosc. Relat. Phenom.* **2016**, *208*, 33.
[41] C. M. Hurd, in: *The Hall Effect in Metals and Alloys* (Ed: C. M. Hurd), Springer US, Boston, MA **1972**, pp. 153.
[42] N. Nagaosa, J. Sinova, S. Onoda, A. H. MacDonald, N. P. Ong, *Rev. Mod. Phys.* **2010**, *82*, 1539.
[43] A. Aharoni, *J. Appl. Phys.* **1998**, *83*, 3432.
[44] T. D. Shen, R. B. Schwarz, J. D. Thompson, *J. Appl. Phys.* **1999**, *85*, 4110.
[45] S. McAlister, I. Shiozaki, C. Hurd, C. Stager, *J. Phys. F* **1981**, *11*, 2129.
[46] D. Gall, *J. Appl. Phys.* **2016**, *119*, 085101.
[47] J. M. Ziman, *Electrons and Phonons: The Theory of Transport Phenomena in Solids*, Oxford University Press, New York, NY, USA **1960**.
[48] Z. Siyuan, Y. Mao, S. Kaito, T. Masaki, U. Shigenori, M. Yoshio, S. Masafumi, U. Rie Yamauchi, K. Ryosuke, K. Takeshi, K. Akio, *J. Phys.* **2015**, *27*, 362201.
[49] V. Kokorin, V. Koledov, V. Shavrov, S. Konoplyuk, S. Thürer, D. Troyanovsky, H. Maier, V. Khovaylo, *J. Appl. Phys.* **2014**, *116*, 103515.
[50] K. A. Borup, E. S. Toberer, L. D. Zoltan, G. Nakatsukasa, M. Errico, J.-P. Fleurial, B. B. Iversen, G. J. Snyder, *Rev. Sci. Instrum.* **2012**, *83*, 123902.
[51] W. M. Haynes, *CRC Handbook of Chemistry and Physics*, 96th edn., CRC Press, Abingdon, UK **2015**.
[52] R. Endo, M. Shima, M. Susa, *Int. J. Thermophys.* **2010**, *31*, **1991**.
[53] W. Fulkerson, J. P. Moore, R. K. Williams, R. S. Graves, D. L. McElroy, *Phys. Rev.* **1968**, *167*, 765.
[54] D. G. Cahill, *Rev. Sci. Instrum.* **1990**, *61*, 802.
[55] J. R. Olson, R. O. Pohl, J. W. Vandersande, A. Zoltan, T. R. Anthony, W. F. Banholzer, *Phys. Rev. B* **1993**, *47*, 14850.
[56] Q. Zheng, S. E. Murray, Z. Diao, A. Bhutani, D. P. Shoemaker, D. G. Cahill, *Phys. Rev. Mater.* **2018**, *2*, 075401.
[57] Q. Zheng, P. V. Braun, D. G. Cahill, *Adv. Mater. Interfaces* **2016**, *3*, 1600234.

